

Article

Efficient Charge Separation and Transport in Fullerene-CuPcOC₈ Donor–Acceptor Nanorod Enhancing Photocatalytic Hydrogen Generation †

Zihui Hua^{1,2}, Bo Wu^{1,2,*}, Yuhe Zhang¹, Chong Wang^{1,2}, Tianyang Dong¹, Yupeng Song^{2,3}, Ying Jiang^{1,2} and Chunru Wang^{1,2,*}

¹ Beijing National Laboratory for Molecular Sciences, Key Laboratory of Molecular Nanostructure and Nanotechnology, Institute of Chemistry, Chinese Academy of Sciences, Beijing 100190, China; zhhuua@iccas.ac.cn (Z.H.); fengyu971008@163.com (Y.Z.); wangchong@iccas.ac.cn (C.W.); dongtianyang006100@163.com (T.D.); jiangying@iccas.ac.cn (Y.J.)

² University of Chinese Academy of Sciences, Beijing 100049, China; songyupeng21@iccas.ac.cn

³ Key Laboratory of Photochemical Conversion and Optoelectronic Materials and CityU-CAS Joint Laboratory of Functional Materials and Devices, Technical Institute of Physics and Chemistry, Chinese Academy of Sciences, Beijing 100190, China

* Correspondence: zkywubo@iccas.ac.cn (B.W.); crwang@iccas.ac.cn (C.W.)

† Dedicated to Professor Chunli Bai on the occasion of his 70th birthday.

Abstract: Photocatalytic hydrogen generation via water decomposition is a promising avenue in the pursuit of large-scale, cost-effective renewable hydrogen energy generation. However, the design of an efficient photocatalyst plays a crucial role in achieving high yields in hydrogen generation. Herein, we have engineered a fullerene-2,3,9,10,16,17,23,24-octa(octyloxy)copper phthalocyanine (C₆₀-CuPcOC₈) photocatalyst, achieving both efficient hydrogen generation and high stability. The significant donor–acceptor (D–A) interactions facilitate the efficient electron transfer from CuPcOC₈ to C₆₀. The rate of photocatalytic hydrogen generation for C₆₀-CuPcOC₈ is 8.32 mmol·g^{−1}·h^{−1}, which is two orders of magnitude higher than the individual C₆₀ and CuPcOC₈. The remarkable increase in hydrogen generation activity can be attributed to the development of a robust internal electric field within the C₆₀-CuPcOC₈ assembly. It is 16.68 times higher than that of the pure CuPcOC₈. The strong internal electric field facilitates the rapid separation within 0.6 ps, enabling photogenerated charge transfer efficiently. Notably, the hydrogen generation efficiency of C₆₀-CuPcOC₈ remains above 95%, even after 10 h, showing its exceptional photocatalytic stability. This study provides critical insight into advancing the field of photocatalysis.

Keywords: fullerenes; internal electric field; charge separation; donor–acceptor structure; photocatalytic hydrogen generation



Citation: Hua, Z.; Wu, B.; Zhang, Y.; Wang, C.; Dong, T.; Song, Y.; Jiang, Y.; Wang, C. Efficient Charge Separation and Transport in Fullerene-CuPcOC₈ Donor–Acceptor Nanorod Enhancing Photocatalytic Hydrogen Generation. *Nanomaterials* **2024**, *14*, 256. <https://doi.org/10.3390/nano14030256>

Academic Editors: Elisa I. García-López and Alessandra Molinari

Received: 18 December 2023

Revised: 1 January 2024

Accepted: 2 January 2024

Published: 24 January 2024



Copyright: © 2024 by the authors. Licensee MDPI, Basel, Switzerland. This article is an open access article distributed under the terms and conditions of the Creative Commons Attribution (CC BY) license (<https://creativecommons.org/licenses/by/4.0/>).

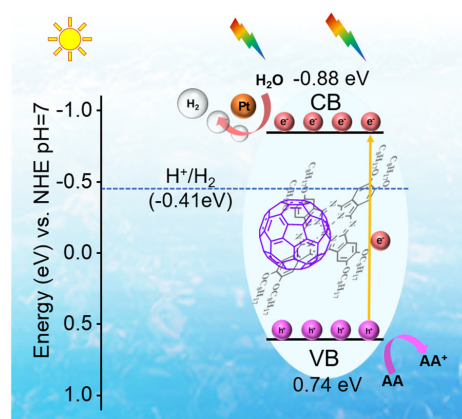
1. Introduction

The photocatalytic decomposition of water, a pivotal process enabling hydrogen generation from solar energy, stands as a promising solution to address the global energy crisis [1–4]. Since the pioneering work on utilizing TiO₂ for hydrogen generation in 1972 [5], the primary research focus in this field has centered on inorganic semiconductors [6–8]. There are inherent defects in most inorganic semiconductor photocatalysts, such as wide forbidden bandwidths, rapid photogenerated carrier recombination, inefficient utilization of sunlight, and photo-corrosion during prolonged light exposure [9]. These restrict their further development and application. Conversely, there has been a recent surge of interest in organic semiconductor photocatalysts owing to their diverse functionalities, various synthesis methods, tunable energy bands, and wide absorption range [10–12]. Various organic semiconductor photocatalysts, including metal–organic frameworks (MOFs) [13], covalent organic frameworks (COFs) [14], graphitic carbon nitride (g-C₃N₄) [15], and linear

conjugated polymers [16], have been utilized in the photocatalytic decomposition of water to produce hydrogen. The main challenge lies in the rational design of highly efficient photocatalysts. It includes the method to optimize their light trapping capability, efficient charge separation and transport, and long-term stability [17].

The donor–acceptor (D–A) structures in organic photocatalysts provide an effective strategy to enhance their catalytic activity [18,19]. Induced by the distinct electron affinities of the donor and acceptor units, the electron push–pull effect facilitates the directed migration of photogenerated electrons from the donor to the acceptor unit. It promotes the separation of photogenerated electrons and holes. This narrowing of the energy band gap of organic photocatalysts through the recombination of the highest occupied molecular orbitals (HOMOs) and the lowest unoccupied molecular orbitals (LUMOs) effectively enhances their light absorption capacity [20]. Moreover, the uneven distribution of positive and negative molecular charges leads to the formation of significant molecular dipole moments [21]. Notably, the magnitude of the molecular dipole moment exhibits a positive correlation with the strength of the internal electric field (IEF). The deliberate establishment of a robust IEF within a molecule effectively facilitates the separation and transportation of photogenerated carriers, making it one of the most efficient methods to enhance photocatalytic activity [22–24].

Fullerenes possess a three-dimensional symmetric structure with exceptional electron-accepting capabilities and commendable physical and chemical stability [25,26]. Copper phthalocyanine (CuPc) is an excellent organic pigment with high chemical stability to light and temperature [27]. CuPc is an effective donor material with remarkable tunability and high visible light absorption [28,29]. Due to these exceptional properties, a series of CuPc photocatalysts have been employed in the field of photocatalytic hydrogen generation [28,30–32]. However, the current efficiency of most Pc-based photocatalysts for hydrogen generation is unsatisfactory. In this study, a novel donor–acceptor (D–A)-type photocatalyst C_{60} -CuPcOC₈ was devised with the aim of enhancing photocatalytic hydrogen generation. C_{60} -CuPcOC₈ demonstrates exceptional hydrogen evolution activity, achieving a rate of 8.32 mmol·g⁻¹·h⁻¹. The introduction of octyloxy modification to CuPc is aimed at enhancing the solubility of phthalocyanine in organic solvents and allowing for the fine-tuning of the physicochemical properties of phthalocyanine derivatives [33]. The non-covalently supramolecular photocatalyst C_{60} -CuPcOC₈ was obtained by using the liquid–liquid interface precipitation method. The hydrogen generation working principal diagram of the C_{60} -CuPcOC₈ assembly is illustrated in Scheme 1. C_{60} -CuPcOC₈ assembly exhibits a broad spectral response range spanning from 300 to 800 nm, allowing efficient utilization of solar energy. Additionally, the C_{60} -CuPcOC₈ manifests a robust IEF owing to the D–A interaction. This robust IEF promotes the efficient separation and transport of photogenerated charges. It can then be expected that C_{60} -CuPcOC₈ photocatalytic hydrogen generation activity will be significantly enhanced.



Scheme 1. The working principle diagram of C_{60} -CuPcOC₈ assembly.

2. Experimental

2.1. C₆₀-CuPcOC₈ Fabrication

The C₆₀-CuPcOC₈ assembly was prepared via the liquid–liquid interfacial precipitation method as shown in Scheme 2. Initially, C₆₀ and CuPcOC₈ powders were dissolved in homo-trimethylbenzene. Subsequently, the solutions were sonicated for 30 min at room temperature. The sonicated solution was then mixed and filtered. Following this, 15 mL isopropanol was added to 5 mL C₆₀-CuPcOC₈ solution. The mixed solution was left to stand for three hours to obtain a precipitate. The resulting precipitate was then filtered and washed three times with methanol. Finally, the desired C₆₀-CuPcOC₈ assembly product was obtained after the vacuum drying. The self-assemblies of C₆₀ and CuPcOC₈ were achieved using an identical method.



Scheme 2. Illustration of preparation process of C₆₀-CuPcOC₈ assembly through the liquid–liquid interface deposition method.

2.2. C₆₀-CuPcOC₈ Characterizations

The powders for assembly or self-assembly were evenly distributed in a sample well. The phase structure was determined using a powder X-ray diffractometer (PXRD) (D/max2550VB/PC, Rigaku, Tokyo, Japan) equipped with Cu K α radiation. The morphological and structure analysis was conducted by field emission scanning electron microscopy (FE-SEM) (Regulus 8100, Hitachi, Tokyo, Japan), transmission electron microscopy (TEM) (HT-7700, Hitachi, Tokyo, Japan), and high-resolution transmission electron microscopy (HRTEM) (JEM-2100F, JEOL, Tokyo, Japan). To conduct SEM testing, the prepared assembly/self-assembly was dispersed in ethanol to form a suspension and then added dropwise onto a silicon wafer. Similarly, TEM testing was performed by adding the suspension dropwise onto a copper microgrid. The UV-Vis diffuse reflectance spectra (DRS) were acquired with a Lambda 1050 UV/VIS/NIR Spectrometer (PerkinElmer, Waltham, MA, USA). The tests were performed with an integrating sphere attachment. The integrating sphere attachment comprised a spherical cavity with an inner wall coated with a highly reflective substance, and BaSO₄ was employed as the standard reflectance material.

2.3. Photocatalytic Hydrogen Generation

The photocatalytic hydrogen generation was conducted employing a 300 W xenon lamp (CEL-HXUV300, CeAulight, Beijing, China) in conjunction with an all-glass automated online trace gas analysis system (Perfect Light Labsolar-6A, PerfectLight, Beijing, China). The dispersion of 5 mg photocatalyst powder in 100 mL of de-ionized water was achieved through ultrasonic treatment.

The ascorbic acid (AA), at a concentration of 0.2 mol·L⁻¹, was employed as a hole sacrificial agent. The hole sacrificial agent can consume photogenerated vacancies. Additionally, 3 wt% Pt was loaded as a co-catalyst on the photocatalysts by photodeposition. Photodeposition is a technique based on light-induced electrochemistry. The process of photodeposition of Pt depends mainly on the photoelectrochemical reaction induced by photocatalysts. The equation for the reductive photodeposition of Pt is as follows.



Evacuating the ambient air from the system was imperative before light irradiation. A 300 W Xe lamp (light intensity: 280 mW/cm^{-2}) with AM 1.5 filter was used as the light source. During light irradiation, continuous stirring of the reaction compounds was maintained using a magnetic stir bar. The system temperature was diligently maintained at 5°C through the circulation of cooling water. The resulting hydrogen yield was quantified using an online gas chromatograph (GC7920, CeAulight, Beijing, China), and argon used as the carrier gas.

Furthermore, monochromatic light with specific wavelengths (400 nm, 420 nm, 450 nm, 500 nm, 550 nm, 600 nm, 650 nm, and 700 nm) was applied from a 300 W xenon lamp to quantify the apparent quantum efficiency (AQE). Average intensity per unit area was determined using a radiometer (CEL-NP2000-2A, CeAulight, Beijing, China), followed by AQE calculation through the subsequent formula:

$$\text{AQE} = \frac{2 \times \text{the number of hydrogen molecules produced}}{\text{the number of incident photon}} \times 100\% \quad (2)$$

2.4. Photoelectrochemical Evaluation

The photoelectrochemical properties were examined using a conventional three-electrode system in combination with an electrochemical workstation (CHI 760e, Chenhua, Shanghai, China). The electrolyte was a 0.5 M Na_2SO_4 solution. The reference electrode was used as a saturated Ag/AgCl electrode, while the counter electrode was a platinum wire. To prepare the working electrode, a dispersion liquid was formed by employing 5 mg of the sample in a solvent mixture of 0.4 mL of water and 0.6 mL of isopropanol. Subsequently, 100 μL of this dispersion liquid was applied onto an ITO glass substrate and subjected to vacuum drying. A light source comprising an AM 1.5 filter using a xenon lamp with a power of 300 W was employed. For electrochemical impedance spectroscopy (EIS), an AC perturbation of 5 mV was applied, spanning a frequency from 10^{-2} to 10^5 Hz. Mott-Schottky plots were generated at frequencies of 500 Hz and 1000 Hz, scan rate of $2 \text{ mV}\cdot\text{s}^{-1}$. Photocurrent response tests were executed under a constant potential of 0.1 V, with illumination by a xenon lamp with a power of 300 W (AM 1.5). The surface photovoltage (SPV) was assessed using the CEL-SPS1000 test system. This system comprises a lock-in amplifier (Stanford), chopper, monochromator (Stanford), and a 500 W xenon lamp as the light source.

2.5. Transient Absorption Experiments

A custom-built spectrometer was employed for conducting femtosecond transient absorption (TA) measurements. The fundamental pulses were obtained from a Ti: Sa amplified laser system (Legend Elite-1K-HE, Coherent, Santa Clara, CA, USA). The laser delivered 25 fs pulses at 1 kHz, and the output was split for white-light continuum generation and optical pumping in the UV region. The excitation wavelength was obtained from a tunable optical parametric amplifier (TOPAS-C, Light Conversion, Vilnius, Lithuania) and selected at 380 nm pump pulse for excitation. The generation of supercontinuum white light with 800 nm pumped CaF_2 results in a spectral window spanning from 350 nm to 800 nm. Control over the delay in time between the pump and probe pulses was achieved through the application of an optical delay stage. A fiber spectrometer (AvaSpec-ULS2048CL-EVO, Avantes, Apeldoorn, The Netherlands) was used to collect visible transient absorption probe signals. Throughout the experiments, the intensity of the 380 nm laser pulses used for pumping was consistently maintained at 400 nJ. Then, the femtosecond TAS data were input into the "Glotaran" software (Glotaran 1.5.1) for global fitting [34,35]. Glotaran is a graphical user interface (GUI) based on the R-package TIMP for global and target analysis of time-resolved spectroscopy. Based on the singular value decomposition (SVD), the evolution-associated spectra were generated using a sequential kinetic model.

3. Results and Discussion

3.1. Morphology and Structural Characterization

A detailed depiction of the morphological characteristics of the C_{60} -CuPcOC₈ is presented in Figure 1. A rod-like structure with diameters ranging from 100 to 150 nm was revealed by SEM. This unique morphology stands in contrast to the individual C_{60} and CuPcOC₈ (Figure S1). Furthermore, a uniform crystal lattice pattern of C_{60} -CuPcOC₈ was elucidated by HRTEM in Figure 1b. The interplanar spacing of C_{60} -CuPcOC₈ was 0.68 nm, 0.99 nm, and 1.47 nm, corresponding to the (301), (101), and (200) crystallographic planes, respectively [36–38]. Subsequently, the PXRD profiles confirm that the identified peaks are 13.4°, 8.96°, and 5.98° (Figure 1c), aligning with the HRTEM analysis.

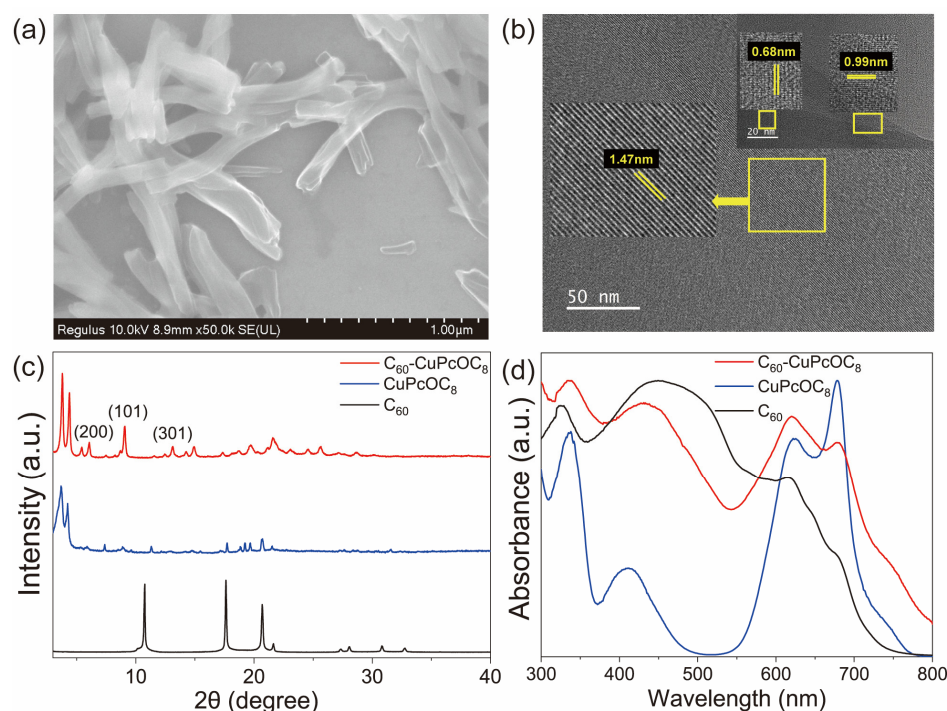


Figure 1. (a) SEM of C_{60} -CuPcOC₈; (b) HRTEM of C_{60} -CuPcOC₈; (c) PXRD of C_{60} , CuPcOC₈, and C_{60} -CuPcOC₈; (d) DRS of C_{60} , CuPcOC₈, and C_{60} -CuPcOC₈.

The molecular frontier orbitals of the C_{60} -CuPcOC₈ are further computed using density functional theory (DFT) at the b3lyp/6-31g(d) level [39]. The HOMO and LUMO of C_{60} -CuPcOC₈ are situated in the phthalocyanine and the C_{60} segment, respectively (Figure S2). This D–A structure is helpful to promote charge separation [40]. A broad absorption spectrum spanning from 300 to 800 nm is exhibited by C_{60} -CuPcOC₈, as demonstrated in the UV-Vis DRS analysis (Figure 1d). In contrast to C_{60} and CuPcOC₈, the absorption onset of C_{60} -CuPcOC₈ undergoes broadening and a red shift. This can be attributed to the strong electron donor–acceptor interactions within C_{60} -CuPcOC₈, as well as the π – π stacking effect that enhances electronic wavefunction conjugation [41].

3.2. Efficient Photocatalytic Activity of the D–A Structure

The molecular orbitals engage in linear interactions via π – π interactions, resulting in the emergence of semiconductor energy bands [42]. The electrochemical Mott–Schottky analysis of C_{60} -CuPcOC₈ reveals positive slopes (Figure S3), indicating the n-type semiconductor. The flat band potential of C_{60} -CuPcOC₈ is estimated to be the conduction band (CB). Importantly, the computed CB value for C_{60} -CuPcOC₈ is -0.88 eV. It meets the thermodynamic conditions for hydrogen generation ($E(H^+/H_2) = -0.41$ eV, pH = 7) compared to the normal hydrogen electrode (NHE) reference at pH 7.

Following the optimization of catalyst and co-catalyst dosages (Figure S4), a notably efficient hydrogen evolution efficiency of $8.32 \text{ mmol}\cdot\text{g}^{-1}\cdot\text{h}^{-1}$ was achieved by employing $\text{C}_{60}\text{-CuPcOC}_8$ across the entire spectrum (Figure 2a). It surpassed the individual CuPcOC_8 or C_{60} by two orders of magnitude (Figure 2b). The solubility of CuPc was improved in organic solvents by modifying CuPc with octyloxy. $\text{C}_{60}\text{-CuPcOC}_8$ assembly was obtained through the interfacial assembly of CuPcOC_8 and C_{60} , leading to a broad spectral absorption range of 300–800 nm. In comparison to other reported phthalocyanine-based organic photocatalysts (as summarized in Table 1), $\text{C}_{60}\text{-CuPcOC}_8$ exhibited remarkable photocatalytic performance, making it a promising candidate for hydrogen generation applications. Furthermore, the apparent quantum efficiency (AQE) of $\text{C}_{60}\text{-CuPcOC}_8$ was evaluated at various wavelengths to evaluate its capability for absorbing visible light. The wavelength-dependent AQE values of $\text{C}_{60}\text{-CuPcOC}_8$ closely paralleled the outcomes obtained from DRS. The trends of the AQE values at different single wavelengths are identical to those of the DRS absorption intensities. The outcomes suggest that the efficiency of light conversion is highly dependent on the range of light response [43].

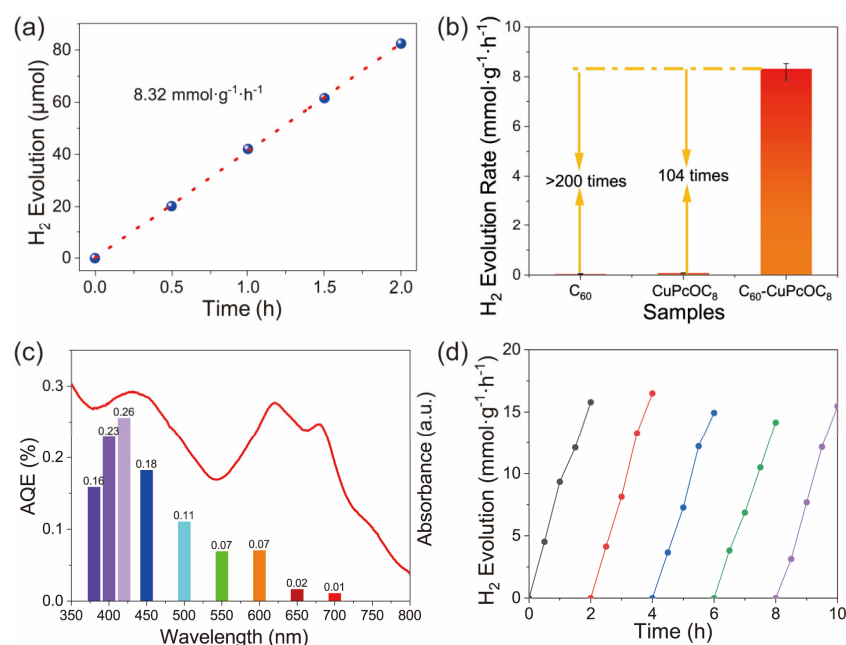


Figure 2. (a) Photocatalytic hydrogen evolution by $\text{C}_{60}\text{-CuPcOC}_8$ under AM 1.5 solar illumination; (b) comparison of photocatalytic hydrogen evolution rate of C_{60} , CuPcOC_8 , and $\text{C}_{60}\text{-CuPcOC}_8$; (c) wavelength-dependent AQE of photocatalytic hydrogen evolution for $\text{C}_{60}\text{-CuPcOC}_8$; (d) cyclic performance assessment of hydrogen evolution of $\text{C}_{60}\text{-CuPcOC}_8$.

Table 1. Summary of the phthalocyanine-based materials for photocatalytic H_2 evolution activity.

Catalyst	Light Source	Hole Sacrificial Agent	Co-Catalyst	H_2 Amount ($\text{mmol g}^{-1}\cdot\text{h}^{-1}$)	References
$\text{C}_{60}\text{-CuPcOC}_8$	AM1.5	AA ^a	Pt	8.32	this work
ZnPc/TiO_2	AM1.5	TEOA ^b	Pt	3.45	[44]
CoPc/TiO_2	AM1.5	TEOA	Pt	3.33	[44]
$\text{N-usRGO}/\text{SiPc}$	UV-vis	TEOA	Pt	0.90	[45]
$\text{MgPc}/\text{mpg-C}_3\text{N}_4$	$\lambda > 400 \text{ nm}$	AA	Pt	0.50	[46]
MnPcG	$\lambda > 420 \text{ nm}$	TEOA	Pt	0.86	[47]
MnPcG	$\lambda > 420 \text{ nm}$	TEOA	-	0.75	[47]
$\text{SiPc}(\text{phenyl})_2\text{G}_2$	UV-vis	TEOA	Pt	1.82	[48]
$\text{SiPc}(\text{phenyl})_2\text{G}_2$	UV-vis	TEOA	-	1.26	[48]
$\text{Zn-tri-PcNc}/\text{g-C}_3\text{N}_4$	$\lambda > 420 \text{ nm}$	TEOA	Pt	8.82	[49]

Table 1. Cont.

Catalyst	Light Source	Hole Sacrificial Agent	Co-Catalyst	H ₂ Amount (mmol g ⁻¹ ·h ⁻¹)	References
Zn-tri-PcNc-1/g-C ₃ N ₄	λ > 500 nm	AA	Pt	4.06	[50]
Zn-tri-PcNc-2/g-C ₃ N ₄	λ > 500 nm	AA	Pt	5.26	[50]
Zn-tri-PcNc-3/g-C ₃ N ₄	λ > 500 nm	AA	Pt	2.02	[50]
Zn-tri-PcNc/TiO ₂	λ > 420 nm	EDTA ^c	Pt	3.78	[51]
CuPc/Zn _{0.5} Cd _{0.5} S	λ > 400 nm	Na ₂ S/Na ₂ SO ₃	-	29.16	[28]
CdS/FePc	AM1.5	lactic acid	-	7.30	[52]
ZnPc-1/TiO ₂	λ > 420 nm	TEOA	Pt	5.39	[53]
ZnPc-2/TiO ₂	λ > 420 nm	TEOA	Pt	2.26	[53]
B _{1.5} HcN-Co _{0.5} %PC	λ > 420 nm	TEOA	Pt	5.56	[54]

^a ascorbic acid, ^b Trolamine, 2,2',2''-Nitrioltriethanol, ^c ethylene diamine tetra-acetic acid.

Furthermore, stability plays a pivotal role in determining the feasibility of photocatalyst recovery and recycling processes. After undergoing five consecutive cycles of photocatalytic evaluation, the photocatalytic effectiveness of C₆₀-CuPcOC₈ was maintained at levels surpassing 95%, with no discernible deactivation observed (Figure 2d). Additionally, the structural integrity was confirmed through characterizations of XRD, XPS, and TEM analyses, as presented in Figure S5. These results emphasize the stability and sustainable nature of C₆₀-CuPcOC₈ as a photocatalyst for hydrogen generation.

3.3. Construction of the D–A Structure Establishes a Robust IEF

The IEF stands as the primary driving force governing the separation and transport of photogenerated charges [55]. A systematic investigation was conducted to understand the precise factors that contribute to the exceptional photocatalytic performance. The electrostatic potential map for C₆₀-CuPcOC₈ is depicted in Figure 3a [56]. The positive potentials are observed at the core of the C₆₀ sphere, while negative potentials are concentrated within the copper phthalocyanine ring. A propensity for charge transfer from CuPcOC₈ to C₆₀ is suggested by this distribution, facilitating charge separation upon photoexcitation. Given the strong donor–acceptor interaction, the calculated dipole moment of the C₆₀-CuPcOC₈ molecular complex is approximately 2.90 Debye. This result is helpful to the formation of a robust IEF. It facilitates the rapid separation of photogenerated charge carriers. The strength of the IEF is quantified using the model developed by Kanataet et al., as illustrated in Figure S6 [57]. Surprisingly, the IEF strength within C₆₀-CuPcOC₈ is 16.86 times higher than CuPcOC₈. This enhancement significantly contributes to the facilitation of the separation and transport of photogenerated charges. Ultimately, it leads to a noteworthy enhancement in the photocatalytic activity for hydrogen generation in C₆₀-CuPcOC₈ compared to CuPcOC₈.

3.4. The D–A Structure Facilitates Charge Separation and Transport

Femtosecond transient absorption spectroscopy (TAS) measurements were conducted to explore the complex kinetics involved in the separation of photogenerated charges. Following laser irradiation at 380 nm, the early femtosecond TAS of C₆₀-CuPcOC₈ reveals excited-state absorption occurring at approximately 540 nm, concurrent with stimulated emission signals observed at 610 nm. Such characteristics are ascribed to the singlet excited state of CuPcOC₈ [58,59]. Following this excited state evolution, a novel set of excited state absorption (ESA) features emerge in close proximity to 560 nm, 710 nm, and 1030 nm in Figure 4b. The distinctive TA peaks within the visible spectrum bear a remarkable resemblance to the CuPcOC₈ cation radicals [60,61]. Simultaneously, the ESA signal was detected at 1030 nm in the near-infrared (NIR) region with the emergence of C₆₀ anion radicals [62]. This offers compelling evidence for the intrinsic occurrence of photo-induced charge separation phenomena within the C₆₀-CuPcOC₈ system. By employing a global analysis, through the utilization of a sequential kinetic model for a comprehensive analysis, three distinct kinetic components are elucidated in Figure 4c,d [63]. The initial phase is

attributed to a “hot” exciton state stemming from the high-energy CuPcOC₈ material within the instrumental response window of approximately ~0.3 picoseconds [64]. Subsequently, this “hot” exciton state expeditiously propels charge separation, occurring within 0.6 ps [65]. The charge-separated state C₆₀^{•-}-CuPcOC₈^{•+} (CS1) state undergoes evolution into a third component within approximately 29 ps, identified as the long-lived charge-separated state C₆₀^{•-}-CuPcOC₈^{•+} (CS2), with a determined lifetime of 0.94 ns. On the contrary, the femtosecond TAS of CuPcOC₈ exhibits characteristics indicative of localized excited states, as illustrated in Figure S7, without charge separation. Therefore, according to the TAS study, ultra-fast and long-lived charge separation do exist in C₆₀-CuPcOC₈.

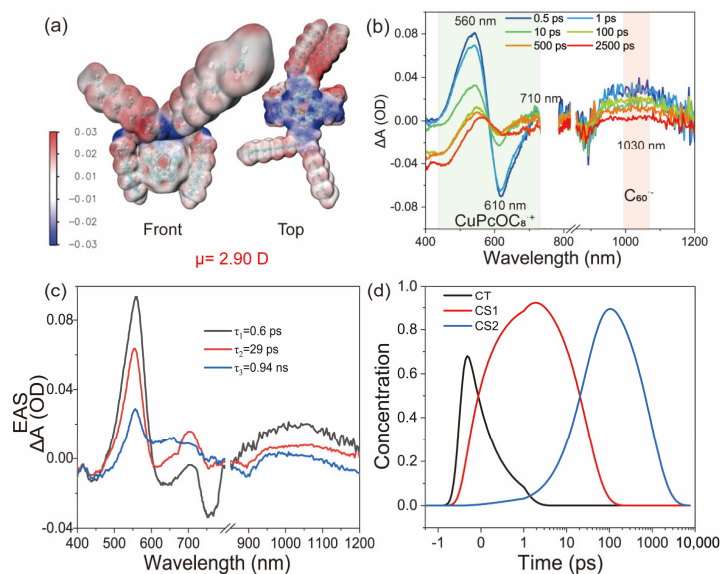


Figure 3. (a) Molecular dipole and electrostatic potential maps of C₆₀-CuPcOC₈ (front and top); (b) femtosecond transient absorption spectra (TAS) of the C₆₀-CuPcOC₈ excited at 380 nm (1×10^{-5} M, aqueous dispersion); (c) evolution-associated spectra (EAS) pertaining to the global analysis of C₆₀-CuPcOC₈; (d) concentrations of different species for the global fit within C₆₀-CuPcOC₈.

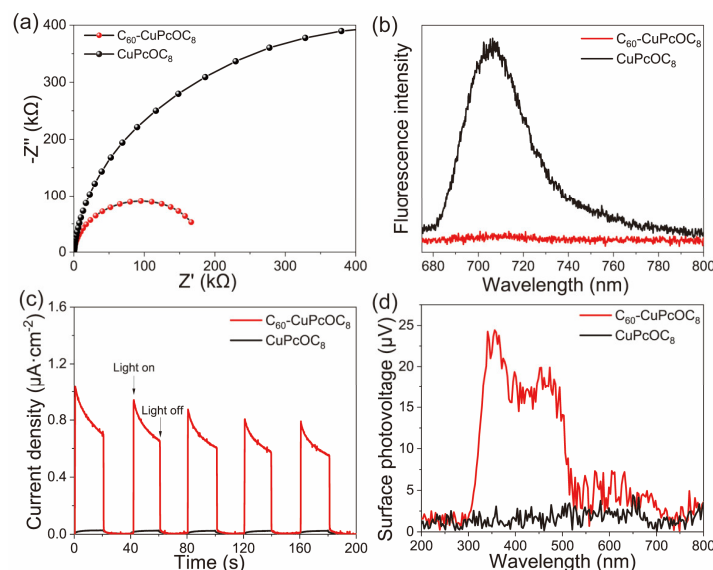


Figure 4. (a) Electrochemical impedance spectra for CuPcOC₈ and C₆₀-CuPcOC₈; (b) emission spectra of fluorescence for CuPcOC₈ and C₆₀-CuPcOC₈; (c) responses of photocurrent for CuPcOC₈ and C₆₀-CuPcOC₈; (d) surface photovoltage profiles for CuPcOC₈ and C₆₀-CuPcOC₈.

Besides charge separation, the charge transport property holds equal significance in the process of photocatalysis. The electrochemical impedance spectra were initially examined in Figure 4a. The charge transfer impedance (R_{ct}) was indicated by the diameter of the arc in the EIS results [66]. Notably, a significantly reduced R_{ct} was observed for C_{60} -CuPcOC₈ compared to CuPcOC₈, effectively enhancing its charge transport capability. Upon exciting the CuPcOC₈ and C_{60} -CuPcOC₈ assemblies at 600 nm, a quenched fluorescence absorption signal was observed from CuPcOC₈ at 710 nm (Figure 4b). This phenomenon was attributed to the promotion of charge separation by the D–A structure of the C_{60} -CuPcOC₈ assemblies. Consequently, the excited electrons no longer underwent radiative transitions but returned to the ground state through a charge transfer or energy transfer process instead. Additionally, the time–current curves of C_{60} -CuPcOC₈ and CuPcOC₈ under steady potential conditions are depicted in Figure 4c. In comparison to CuPcOC₈, a more robust photocurrent response is exhibited by C_{60} -CuPcOC₈. The enhanced response is attributed to the improvement of charge transfer efficiency. In the surface photovoltage (SPV) spectrum (Figure 4d), a significantly elevated positive photovoltage signal is observed in the 300 to 520 nm range for C_{60} -CuPcOC₈. Notably, this signal is approximately ten times stronger than that observed in CuPcOC₈. This notable difference implies a substantial increase in the migration of photogenerated charges toward the surface within the C_{60} -CuPcOC₈ assembly.

Drawing upon the preceding discussion, a plausible mechanism for the photocatalytic is proposed in Figure 5. The strong D–A interactions of C_{60} -CuPcOC₈ play a pivotal role in establishing a robust IEF. The robust IEF facilitates charge separation and transfer. Photogenerated electrons migrate to the surface, accelerating a reduction reaction yielding hydrogen, wherein Pt functions as a co-catalyst. Concurrently, the photogenerated holes engage in reactions with the sacrificial agent, ascorbic acid. In brief, the C_{60} -CuPcOC₈ system achieves efficient separation of photogenerated electron–hole pairs, resulting in an efficient photocatalytic hydrogen generation.

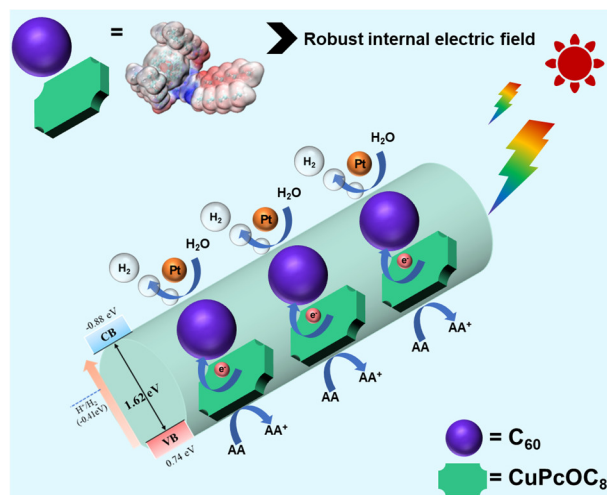


Figure 5. Schematic mechanism of photocatalytic reactions of the C_{60} -CuPcOC₈.

4. Conclusions

In summary, we have utilized the light-harvesting CuPcOC₈ donor and efficient-electron-transport C_{60} acceptor to synthesize a novel photocatalyst, C_{60} -CuPcOC₈. The photocatalyst exhibits a broad spectral absorption range spanning from 300 to 800 nm, facilitating excellent photocatalytic hydrogen generation. The incorporation of a D–A architecture within C_{60} -CuPcOC₈ results in a larger molecular dipole moment, facilitating the creation of a robust IEF. This IEF promoted the separation and transportation of the photogenerated charge carriers. Consequently, C_{60} -CuPcOC₈ demonstrates exceptional hydrogen evolution activity, achieving a rate of $8.32 \text{ mmol} \cdot \text{g}^{-1} \cdot \text{h}^{-1}$. This rate surpasses

that of C₆₀ and CuPcOC₈ monomers by two orders of magnitude. This research introduces a novel approach for designing highly active supramolecular photocatalytic materials, offering valuable insights for the construction of an efficient photocatalytic hydrogen generation system.

Supplementary Materials: The following supporting information can be downloaded at: <https://www.mdpi.com/article/10.3390/nano14030256/s1>, Figure S1. SEM for (a) C₆₀ and (b) CuPcOC₈; Figure S2. (a) LUMO and (b) HOMO of C₆₀-CuPcOC₈; Figure S3. (a) Tauc-plots of C₆₀-CuPcOC₈, (b) Mott–Schottky plots of C₆₀-CuPcOC₈, (c) schematic representation of the redox potential of C₆₀-CuPcOC₈; Figure S4. Photocatalytic H₂ evolution rate of C₆₀-CuPcOC₈ with varied (a) weight and (b) loading amount of Pt under full-spectrum light; Figure S5. (a) PXRD of C₆₀-CuPcOC₈ before and after photocatalytic hydrogen generation; (b) Cu elemental XPS of C₆₀-CuPcOC₈ before and after photocatalytic hydrogen generation; HRTEM of C₆₀-CuPcOC₈ (c) before and (d) after photocatalytic hydrogen generation; Figure S6. Surface charge density of (a) CuPcOC₈ and (b) C₆₀-CuPcOC₈; Figure S7. Evolution-associated spectra (EAS) of the CuPcOC₈ at 380 nm (1 × 10⁻⁵ M, aqueous dispersion).

Author Contributions: Conceptualization, B.W. and C.W. (Chunru Wang); methodology, Z.H. and Y.Z.; validation, Z.H. and B.W.; formal analysis, Z.H., C.W. (Chong Wang), T.D., Y.S. and Y.J.; investigation, Z.H. and Y.Z.; resources, B.W. and C.W. (Chunru Wang); data curation, Z.H.; writing—original draft preparation, Z.H.; writing—review and editing, B.W.; supervision, C.W. (Chunru Wang); project administration, B.W. and C.W. (Chunru Wang); funding acquisition, B.W. and C.W. (Chunru Wang). All authors have read and agreed to the published version of the manuscript.

Funding: This work was supported by the National Natural Science Foundation of China (52072374, 52322204, 51832008) and the Ministry of Science and Technology of China (2022YFA1205900). B. Wu particularly thanks the Youth Innovation Promotion Association of CAS (Y2022015).

Institutional Review Board Statement: Not applicable.

Informed Consent Statement: Not applicable.

Data Availability Statement: The data presented in this study are available upon reasonable request from the corresponding author.

Acknowledgments: Thank you to Jing Li at the Technical Institute of Physics and Chemistry, Chinese Academy of Sciences, for the help with transient absorption measurements. Thank you to Jing Tai at the Institute of Chemistry, Chinese Academy of Sciences, for the valuable assistance in obtaining high-resolution transmission electron microscope images.

Conflicts of Interest: The authors declare no conflict of interest.

References

1. Xu, Q.; Zhang, L.; Cheng, B.; Fan, J.; Yu, J. S-Scheme Heterojunction Photocatalyst. *Chem* **2020**, *6*, 1543–1559. [[CrossRef](#)]
2. Liang, Y.; Li, T.; Lee, Y.; Zhang, Z.; Li, Y.; Si, W.; Liu, Z.; Zhang, C.; Qiao, Y.; Bai, S.; et al. Organic Photovoltaic Catalyst with Σ - π Anchor for High-Performance Solar Hydrogen Evolution. *Angew. Chem. Int. Ed.* **2023**, *62*, e202217989. [[CrossRef](#)] [[PubMed](#)]
3. Zhu, Y.; Zhang, Z.; Si, W.; Sun, Q.; Cai, G.; Li, Y.; Jia, Y.; Lu, X.; Xu, W.; Zhang, S.; et al. Organic Photovoltaic Catalyst with Extended Exciton Diffusion for High-Performance Solar Hydrogen Evolution. *J. Am. Chem. Soc.* **2022**, *144*, 12747–12755. [[CrossRef](#)] [[PubMed](#)]
4. Liu, A.; Gedda, L.; Axelsson, M.; Pavliuk, M.; Edwards, K.; Hammarström, L.; Tian, H. Panchromatic Ternary Polymer Dots Involving Sub-Picosecond Energy and Charge Transfer for Efficient and Stable Photocatalytic Hydrogen Evolution. *J. Am. Chem. Soc.* **2021**, *143*, 2875–2885. [[CrossRef](#)] [[PubMed](#)]
5. Fujishima, A.; Honda, K. Electrochemical Photolysis of Water at a Semiconductor Electrode. *Nature* **1972**, *238*, 37–38. [[CrossRef](#)] [[PubMed](#)]
6. Rabell, G.O.; Cruz, M.R.A.; Juárez-Ramírez, I. Hydrogen Production of ZnO and ZnO/Ag Films by Photocatalysis and Photoelectrocatalysis. *Mater. Sci. Semicond. Process.* **2021**, *134*, 105985. [[CrossRef](#)]
7. Lange, T.; Reichenberger, S.; Ristig, S.; Rohe, M.; Strunk, J.; Barcikowski, S.; Schlögl, R. Zinc Sulfide for Photocatalysis: White Angel or Black Sheep? *Prog. Mater. Sci.* **2022**, *124*, 100865. [[CrossRef](#)]
8. Liang, Z.; Ouyang, B.; Wang, T.; Liu, X.; Huo, H.; Liu, D.; Feng, H.; Ma, J.; Deng, K.; Li, A.; et al. Pt Modified TiO₂/NiO p-n Junction with Enhanced Surface Reaction and Charge Separation for Efficient Photocatalytic Hydrogen Evolution. *Int. J. Hydrogen Energy* **2022**, *47*, 10868–10876. [[CrossRef](#)]

9. Qi, M.-Y.; Conte, M.; Anpo, M.; Tang, Z.-R.; Xu, Y.-J. Cooperative Coupling of Oxidative Organic Synthesis and Hydrogen Production over Semiconductor-Based Photocatalysts. *Chem. Rev.* **2021**, *121*, 13051–13085. [[CrossRef](#)]
10. Niu, P.; Dai, J.; Zhi, X.; Xia, Z.; Wang, S.; Li, L. Photocatalytic Overall Water Splitting by Graphitic Carbon Nitride. *InfoMat* **2021**, *3*, 931–961. [[CrossRef](#)]
11. Banerjee, T.; Podjaski, F.; Kröger, J.; Biswal, B.P.; Lotsch, B.V. Polymer Photocatalysts for Solar-to-Chemical Energy Conversion. *Nat. Rev. Mater.* **2020**, *6*, 168–190. [[CrossRef](#)]
12. Ghosh, S.; Nakada, A.; Springer, M.A.; Kawaguchi, T.; Suzuki, K.; Kaji, H.; Baburin, I.; Kuc, A.; Heine, T.; Suzuki, H.; et al. Identification of Prime Factors to Maximize the Photocatalytic Hydrogen Evolution of Covalent Organic Frameworks. *J. Am. Chem. Soc.* **2020**, *142*, 9752–9762. [[CrossRef](#)] [[PubMed](#)]
13. Lu, L.; Wu, B.; Shi, W.; Cheng, P. Metal–Organic Framework-Derived Heterojunctions as Nanocatalysts for Photocatalytic Hydrogen Production. *Inorg. Chem. Front.* **2019**, *6*, 3456–3467. [[CrossRef](#)]
14. Wang, X.; Chen, L.; Chong, S.Y.; Little, M.A.; Wu, Y.; Zhu, W.-H.; Clowes, R.; Yan, Y.; Zwijnenburg, M.A.; Sprick, R.S.; et al. Sulfone-Containing Covalent Organic Frameworks for Photocatalytic Hydrogen Evolution from Water. *Nat. Chem.* **2018**, *10*, 1180–1189. [[CrossRef](#)] [[PubMed](#)]
15. Zhu, Q.; Xu, Z.; Qiu, B.; Xing, M.; Zhang, J. Emerging Cocatalysts on g-C₃N₄ for Photocatalytic Hydrogen Evolution. *Small* **2021**, *17*, 2101070. [[CrossRef](#)] [[PubMed](#)]
16. Zhao, C.; Chen, Z.; Shi, R.; Yang, X.; Zhang, T. Recent Advances in Conjugated Polymers for Visible-Light-Driven Water Splitting. *Adv. Mater.* **2020**, *32*, 1907296. [[CrossRef](#)]
17. Tong, H.; Ouyang, S.; Bi, Y.; Umezawa, N.; Oshikiri, M.; Ye, J. Nano-Photocatalytic Materials: Possibilities and Challenges. *Adv. Mater.* **2012**, *24*, 229–251. [[CrossRef](#)]
18. Kosco, J.; Bidwell, M.; Cha, H.; Martin, T.; Howells, C.T.; Sachs, M.; Anjum, D.H.; Gonzalez Lopez, S.; Zou, L.; Wadsworth, A.; et al. Enhanced Photocatalytic Hydrogen Evolution from Organic Semiconductor Heterojunction Nanoparticles. *Nat. Mater.* **2020**, *19*, 559–565. [[CrossRef](#)]
19. Yang, J.; Jing, J.; Zhu, Y. A Full-spectrum Porphyrin–Fullerene D–A Supramolecular Photocatalyst with Giant Built-in Electric Field for Efficient Hydrogen Production. *Adv. Mater.* **2021**, *33*, 2101026. [[CrossRef](#)]
20. Yang, Q.; Luo, M.; Liu, K.; Cao, H.; Yan, H. Covalent Organic Frameworks for Photocatalytic Applications. *Appl. Catal. B* **2020**, *276*, 119174. [[CrossRef](#)]
21. Yao, H.; Qian, D.; Zhang, H.; Qin, Y.; Xu, B.; Cui, Y.; Yu, R.; Gao, F.; Hou, J. Critical Role of Molecular Electrostatic Potential on Charge Generation in Organic Solar Cells: Critical Role of Molecular Electrostatic Potential on Charge Generation in Organic Solar Cells. *Chin. J. Chem.* **2018**, *36*, 491–494. [[CrossRef](#)]
22. Guo, Y.; Zhou, Q.; Nan, J.; Shi, W.; Cui, F.; Zhu, Y. Perylenetetracarboxylic Acid Nanosheets with Internal Electric Fields and Anisotropic Charge Migration for Photocatalytic Hydrogen Evolution. *Nat. Commun.* **2022**, *13*, 2067. [[CrossRef](#)] [[PubMed](#)]
23. Deng, A.; Sun, Y.; Gao, Z.; Yang, S.; Liu, Y.; He, H.; Zhang, J.; Liu, S.; Sun, H.; Wang, S. Internal Electric Field in Carbon Nitride-Based Heterojunctions for Photocatalysis. *Nano Energy* **2023**, *108*, 108228. [[CrossRef](#)]
24. Zhou, Q.; Guo, Y.; Ye, Z.; Fu, Y.; Guo, Y.; Zhu, Y. Carbon Nitride Photocatalyst with Internal Electric Field Induced Photogenerated Carriers Spatial Enrichment for Enhanced Photocatalytic Water Splitting. *Mater. Today* **2022**, *58*, 100–109. [[CrossRef](#)]
25. Pan, Y.; Liu, X.; Zhang, W.; Liu, Z.; Zeng, G.; Shao, B.; Liang, Q.; He, Q.; Yuan, X.; Huang, D.; et al. Advances in Photocatalysis Based on Fullerene C₆₀ and Its Derivatives: Properties, Mechanism, Synthesis, and Applications. *Appl. Catal. B* **2020**, *265*, 118579. [[CrossRef](#)]
26. Huo, J.; Zeng, H. A Novel Triphenylamine Functionalized Bithiazole–Metal Complex with C₆₀ for Photocatalytic Hydrogen Production under Visible Light Irradiation. *J. Mater. Chem. A* **2015**, *3*, 6258–6264. [[CrossRef](#)]
27. Guo, Z.; Chen, B.; Zhang, M.; Mu, J.; Shao, C.; Liu, Y. Zinc Phthalocyanine Hierarchical Nanostructure with Hollow Interior Space: Solvent–Thermal Synthesis and High Visible Photocatalytic Property. *J. Colloid Interface Sci.* **2010**, *348*, 37–42. [[CrossRef](#)]
28. Yang, Q.; Zhu, H.; Ji, X.; Zhang, Y.; Yu, L. Nanoarchitectonics of Core-Shelled Hollow CuPc/Zn_{0.5}Cd_{0.5}S Photocatalyst for Stable Hydrogen Evolution under Visible-Light Irradiation. *J. Alloys Compd.* **2022**, *926*, 166890. [[CrossRef](#)]
29. Keizer, S.P.; Mack, J.; Bench, B.A.; Gorun, S.M.; Stillman, M.J. Spectroscopy and Electronic Structure of Electron Deficient Zinc Phthalocyanines. *J. Am. Chem. Soc.* **2003**, *125*, 7067–7085. [[CrossRef](#)]
30. Moon, H.S.; Yong, K. Noble-Metal Free Photocatalytic Hydrogen Generation of CuPc/TiO₂ Nanoparticles under Visible-Light Irradiation. *Appl. Surf. Sci.* **2020**, *530*, 147215. [[CrossRef](#)]
31. Keshipour, S.; Mohammad-Alizadeh, S.; Razeghi, M.H. Copper Phthalocyanine@graphene Oxide as a Cocatalyst of TiO₂ in Hydrogen Generation. *J. Phys. Chem. Solids* **2022**, *161*, 110434. [[CrossRef](#)]
32. Men, C.; Chen, L.; Ji, H.; Qin, Z.; Su, T. Synergistic Effect of Internal Electric Field and Ligand-to-Metal Charge Transfer in Z-Scheme CuPc/ZnIn₂S₄ for Boosting Photocatalytic Hydrogen Evolution. *Chem. Eng. J.* **2023**, *473*, 145173. [[CrossRef](#)]
33. Vadakel, V.T.; Menon, C.S. Optical and Surface Morphological Studies on CuPcOC₈ Thin Films Prepared by Physical Vapour Deposition. *Mater. Sci.-Pol.* **2013**, *31*, 391–396. [[CrossRef](#)]
34. Mullen, K.M.; Stokkum, I.H.M.V. TIMP: An R Package for Modeling Multi-Way Spectroscopic Measurements. *J. Stat. Softw.* **2007**, *18*, 1–46. [[CrossRef](#)]
35. Van Stokkum, I.H.M.; Larsen, D.S.; Van Grondelle, R. Global and Target Analysis of Time-Resolved Spectra. *Biochim. Biophys. Acta Bioenerg.* **2004**, *1657*, 82–104. [[CrossRef](#)] [[PubMed](#)]

36. Tang, Q.; Li, H.; Liu, Y.; Hu, W. High-Performance Air-Stable n-Type Transistors with an Asymmetrical Device Configuration Based on Organic Single-Crystalline Submicrometer/Nanometer Ribbons. *J. Am. Chem. Soc.* **2006**, *128*, 14634–14639. [[CrossRef](#)] [[PubMed](#)]
37. Ai, X.; Lin, J.; Chang, Y.; Zhou, L.; Zhang, X.; Qin, G. Phase Modification of Copper Phthalocyanine Semiconductor by Converting Powder to Thin Film. *Appl. Surf. Sci.* **2018**, *428*, 788–792. [[CrossRef](#)]
38. Warner, M.; Mauthoor, S.; Felton, S.; Wu, W.; Gardener, J.A.; Din, S.; Klose, D.; Morley, G.W.; Stoneham, A.M.; Fisher, A.J.; et al. Spin-Based Diagnostic of Nanostructure in Copper Phthalocyanine–C₆₀ Solar Cell Blends. *ACS Nano* **2012**, *6*, 10808–10815. [[CrossRef](#)]
39. Yanai, T.; Tew, D.P.; Handy, N.C. A New Hybrid Exchange–Correlation Functional Using the Coulomb-Attenuating Method (CAM-B3LYP). *Chem. Phys. Lett.* **2004**, *393*, 51–57. [[CrossRef](#)]
40. Lim, H.; Yang, S.; Lee, S.-H.; Lee, J.-Y.; Lee, Y.; Situmorang, A.B.; Kim, Y.-H.; Kim, J.W. Influence of the Metal Phthalocyanine Molecular Orientation on Charge Separation at the Organic Donor/Acceptor Interface. *J. Mater. Chem. C* **2021**, *9*, 2156–2164. [[CrossRef](#)]
41. Heutz, S.; Sullivan, P.; Sanderson, B.M.; Schultes, S.M.; Jones, T.S. Influence of Molecular Architecture and Intermixing on the Photovoltaic, Morphological and Spectroscopic Properties of CuPc–C₆₀ Heterojunctions. *Sol. Energy Mater. Sol. Cells* **2004**, *83*, 229–245. [[CrossRef](#)]
42. Saito, G.; Yoshida, Y. Development of Conductive Organic Molecular Assemblies: Organic Metals, Superconductors, and Exotic Functional Materials. *Bull. Chem. Soc. Jpn.* **2007**, *80*, 1–137. [[CrossRef](#)]
43. Chen, C.; Xiong, Y.; Zhong, X.; Lan, P.C.; Wei, Z.; Pan, H.; Su, P.; Song, Y.; Chen, Y.; Nafady, A.; et al. Enhancing Photocatalytic Hydrogen Production via the Construction of Robust Multivariate Ti-MOF/COF Composites. *Angew. Chem. Int. Ed.* **2022**, *61*, e202114071. [[CrossRef](#)] [[PubMed](#)]
44. Genc, E.; Yüzer, A.C.; Yanalak, G.; Harputlu, E.; Aslan, E.; Ocakoglu, K.; Ince, M.; Patir, I.H. The Effect of Central Metal in Phthalocyanine for Photocatalytic Hydrogen Evolution via Artificial Photosynthesis. *Renew. Energy* **2020**, *162*, 1340–1346. [[CrossRef](#)]
45. Huang, J.; Wu, Y.; Wang, D.; Ma, Y.; Yue, Z.; Lu, Y.; Zhang, M.; Zhang, Z.; Yang, P. Silicon Phthalocyanine Covalently Functionalized N-Doped Ultrasmall Reduced Graphene Oxide Decorated with Pt Nanoparticles for Hydrogen Evolution from Water. *ACS Appl. Mater. Interfaces* **2015**, *7*, 3732–3741. [[CrossRef](#)]
46. Takanebe, K.; Kamata, K.; Wang, X.; Antonietti, M.; Kubota, J.; Domen, K. Photocatalytic Hydrogen Evolution on Dye-Sensitized Mesoporous Carbon Nitride Photocatalyst with Magnesium Phthalocyanine. *Phys. Chem. Chem. Phys.* **2010**, *12*, 13020. [[CrossRef](#)]
47. Wang, D.; Huang, J.; Li, X.; Yang, P.; Du, Y.; Goh, C.M.; Lu, C. Photocatalytic H₂ Production under Visible-Light Irradiation Based on Covalent Attachment of Manganese Phthalocyanine to Graphene. *J. Mater. Chem. A* **2015**, *3*, 4195–4202. [[CrossRef](#)]
48. Xiao, B.; Zhu, M.; Li, X.; Yang, P.; Qiu, L.; Lu, C. A Stable and Efficient Photocatalytic Hydrogen Evolution System Based on Covalently Linked Silicon-Phthalocyanine-Graphene with Surfactant. *Int. J. Hydrogen Energy* **2016**, *41*, 11537–11546. [[CrossRef](#)]
49. Zhang, X.; Peng, T.; Yu, L.; Li, R.; Li, Q.; Li, Z. Visible/Near-Infrared-Light-Induced H₂ Production over g-C₃N₄ Co-Sensitized by Organic Dye and Zinc Phthalocyanine Derivative. *ACS Catal.* **2015**, *5*, 504–510. [[CrossRef](#)]
50. Zhang, X.; Yu, L.; Li, R.; Peng, T.; Li, X. Asymmetry and Electronic Directionality: A Means of Improving the Red/near-IR-Light-Responsive Photoactivity of Phthalocyanine-Sensitized Carbon Nitride. *Catal. Sci. Technol.* **2014**, *4*, 3251. [[CrossRef](#)]
51. Zhang, X.; Yu, L.; Zhuang, C.; Peng, T.; Li, R.; Li, X. Highly Efficient Visible/near-IR-Light-Driven Photocatalytic H₂ Production over Asymmetric Phthalocyanine-Sensitized TiO₂. *RSC Adv.* **2013**, *3*, 14363. [[CrossRef](#)]
52. Zhang, W.; Zhou, X.; Huang, J.; Zhang, S.; Xu, X. Noble Metal-Free Core-Shell CdS/Iron Phthalocyanine Z-Scheme Photocatalyst for Enhancing Photocatalytic Hydrogen Evolution. *J. Mater. Sci. Technol.* **2022**, *115*, 199–207. [[CrossRef](#)]
53. Genc Acar, E.; Yüzer, A.C.; Kurtay, G.; Yanalak, G.; Harputlu, E.; Aslan, E.; Ocakoglu, K.; Güllü, M.; Ince, M.; Patir, I.H. Improving the Photocatalytic Hydrogen Generation Using Nonaggregated Zinc Phthalocyanines. *ACS Appl. Energy Mater.* **2021**, *4*, 10222–10233. [[CrossRef](#)]
54. Miao, X.; Wang, B.; Fan, H.; Zhang, P.; Bai, S.; Liu, W. Tremella-like Boron-Doped Hierarchical CN and Dispersion Co Phthalocyanine Assembling Heterojunction for Photocatalytic Hydrogen Evolution. *Chem. Eng. J.* **2023**, *465*, 142775. [[CrossRef](#)]
55. Yue, X.; Fan, J.; Xiang, Q. Internal Electric Field on Steering Charge Migration: Modulations, Determinations and Energy-Related Applications. *Adv. Funct. Mater.* **2022**, *32*, 2110258. [[CrossRef](#)]
56. Lu, T.; Chen, F. Multiwfn: A Multifunctional Wavefunction Analyzer. *J. Comput. Chem.* **2012**, *33*, 580–592. [[CrossRef](#)] [[PubMed](#)]
57. Xi, Y.; Chen, W.; Dong, W.; Fan, Z.; Wang, K.; Shen, Y.; Tu, G.; Zhong, S.; Bai, S. Engineering an Interfacial Facet of S-Scheme Heterojunction for Improved Photocatalytic Hydrogen Evolution by Modulating the Internal Electric Field. *ACS Appl. Mater. Interfaces* **2021**, *13*, 39491–39500. [[CrossRef](#)]
58. Huang, P.; Hernández, A.; Kazim, S.; Follana-Berná, J.; Ortiz, J.; Lezama, L.; Sastre-Santos, Á.; Ahmad, S. Asymmetrically Substituted Phthalocyanines as Dopant-Free Hole Selective Layers for Reliability in Perovskite Solar Cells. *ACS Appl. Energy Mater.* **2021**, *4*, 10124–10135. [[CrossRef](#)]
59. Jin, S.; Supur, M.; Addicoat, M.; Furukawa, K.; Chen, L.; Nakamura, T.; Fukuzumi, S.; Irle, S.; Jiang, D. Creation of Superheterojunction Polymers via Direct Polycondensation: Segregated and Bicontinuous Donor–Acceptor π -Columnar Arrays in Covalent Organic Frameworks for Long-Lived Charge Separation. *J. Am. Chem. Soc.* **2015**, *137*, 7817–7827. [[CrossRef](#)]

60. Padgaonkar, S.; Amsterdam, S.H.; Bergeron, H.; Su, K.; Marks, T.J.; Hersam, M.C.; Weiss, E.A. Molecular-Orientation-Dependent Interfacial Charge Transfer in Phthalocyanine/MoS₂ Mixed-Dimensional Heterojunctions. *J. Phys. Chem. C* **2019**, *123*, 13337–13343. [[CrossRef](#)]
61. El-Khouly, M.E.; Kang, E.S.; Kay, K.-Y.; Choi, C.S.; Aaraki, Y.; Ito, O. Silicon-Phthalocyanine-Cored Fullerene Dendrimers: Synthesis and Prolonged Charge-Separated States with Dendrimer Generations. *Chem. Eur. J.* **2007**, *13*, 2854–2863. [[CrossRef](#)] [[PubMed](#)]
62. Chai, Y.; Liu, X.; Wu, B.; Liu, L.; Wang, Z.; Weng, Y.; Wang, C. In Situ Switching of Photoinduced Electron Transfer Direction by Regulating the Redox State in Fullerene-Based Dyads. *J. Am. Chem. Soc.* **2020**, *142*, 4411–4418. [[CrossRef](#)] [[PubMed](#)]
63. Binsl, T.W.; Mullen, K.M.; Stokkum, I.H.M.V.; Heringa, J.; Beek, J.H.G.M.V. FluxSimulator: An R Package to Simulate Isotopomer Distributions in Metabolic Networks. *J. Stat. Softw.* **2007**, *18*, 1–17. [[CrossRef](#)]
64. Liu, L.P.; Chen, X.J.; Chai, Y.Q.; Zhang, W.N.; Liu, X.L.; Zhao, F.W.; Wang, Z.; Weng, Y.X.; Wu, B.; Geng, H.; et al. Highly Efficient Photocatalytic Hydrogen Production via Porphyrin-Fullerene Supramolecular Photocatalyst with Donor-Acceptor Structure. *Chem. Eng. J.* **2022**, *444*, 136621. [[CrossRef](#)]
65. Savoie, B.M.; Rao, A.; Bakulin, A.A.; Gelinias, S.; Movaghar, B.; Friend, R.H.; Marks, T.J.; Ratner, M.A. Unequal Partnership: Asymmetric Roles of Polymeric Donor and Fullerene Acceptor in Generating Free Charge. *J. Am. Chem. Soc.* **2014**, *136*, 2876–2884. [[CrossRef](#)]
66. Wang, W.-R.; Li, J.; Li, Q.; Xu, Z.-W.; Liu, L.-N.; Chen, X.-Q.; Xiao, W.-J.; Yao, J.; Zhang, F.; Li, W.-S. Side-Chain-Extended Conjugation: A Strategy for Improving the Photocatalytic Hydrogen Production Performance of a Linear Conjugated Polymer. *J. Mater. Chem. A* **2021**, *9*, 8782–8791. [[CrossRef](#)]

Disclaimer/Publisher's Note: The statements, opinions and data contained in all publications are solely those of the individual author(s) and contributor(s) and not of MDPI and/or the editor(s). MDPI and/or the editor(s) disclaim responsibility for any injury to people or property resulting from any ideas, methods, instructions or products referred to in the content.